INORGANIC CHEMISTRY FRONTIERS

RESEARCH ARTICLE

View Article Online
View Journal | View Issue

Check for updates

Cite this: *Inorg. Chem. Front.*, 2024, **11**, 8813

Large optical anisotropy in noncentrosymmetric phosphate with pseudo 2D intercalated layer†

Qiao Xia,‡[a] Xingxing Jiang,‡[b] Lu Qi,‡[a] Chao Wu,*[a] Zheshuai Lin,[b] Zhipeng Huang,[a] Mark G. Humphrey,[c] Kazuyuki Tatsumi[a,d] and Chi Zhang*[a]

Received 5th September 2024,
Accepted 20th October 2024

DOI: 10.1039/d4qi02245a

rsc.li/frontiers-inorganic

On account of the high T_d symmetry of the optically active [PO_4] motif, the birefringence of ultraviolet (UV) nonlinear optical (NLO) phosphates is extremely small. Here, two UV-transparent phosphates ($C_4H_7N_2$)(H_2PO_4) and ($C_3H_5N_2$)(H_2PO_4) exhibiting pseudo two-dimensional (2D) intercalated layers were successfully synthesized by simultaneously introducing planar and tetrahedral motifs. The arrangements of planar and tetrahedral motifs within the pseudo 2D intercalated layers change from the inverse pairing mode to the uniform pairing mode, resulting in the structural evolution from centrosymmetric (CS) ($C_4H_7N_2$)(H_2PO_4) to noncentrosymmetric (NCS) ($C_3H_5N_2$)(H_2PO_4). Compared with the CS phosphate ($C_4H_7N_2$)(H_2PO_4) (0.12 at 546 nm, 5.21 eV), the NCS ($C_3H_5N_2$)(H_2PO_4) exhibits larger birefringence (0.15 at 546 nm), a blue-shifted band gap (5.41 eV), and a phase-matching second harmonic generation. Structural analysis and first-principles calculations indicate that the large birefringence in the ($C_3H_5N_2$)(H_2PO_4) crystal is caused by the closely antiparallel arrangement between adjacent pseudo 2D intercalated layers, in which the planar $(C_3H_5N_2)^+$ motifs play a dominant role in optical properties.

Published on 22 Oktober 2024. Downloaded on 14.10.25 16:33:10.

1. Introduction

Birefringence (Δn) and optical band gap (E_g) are two important performance parameters of nonlinear optical (NLO) crystals since they can influence the phase-matching ability of the crystals and determine the wavelength region of the crystals.[1–12] The non-π-conjugated [PO_4] motif is one of the most promising building blocks for NLO materials. The resultant phosphates include well-known NLO crystals, such as inorganic KH_2PO_4 (KDP),[13] $KTiOPO_4$ (KTP)[14] and semi-organic $(H_2N)_2CNH(CH_2)_3CH(NH_3)COO{\cdot}H_2PO_4{\cdot}H_2O$ (LAP),[15] as well as newly developed $Ba_3P_3O_{10}X$ (X = Cl, Br),[16] $AMgPO_4{\cdot}6H_2O$ (A = Rb, Cs, NH_4, K),[17,18] $K_4Mg_4(P_2O_7)_3$,[19] $LiCs_2PO_4$,[20] and $RbNaMgP_2O_7$.[21] Unfortunately, the T_d symmetry of the tetrahedral [PO_4] motif hinders the response of polarizability anisotropy, which seriously impedes phase-matching ability and thus affects the application of second harmonic generation (SHG). From the perspective of structure determining performance, structural motifs with large polarizability anisotropy are a prerequisite for materials to obtain large birefringence, and the key to achieving large birefringence lies in the oriented arrangement of structural motifs with large optical anisotropy in the lattice or the utilization of low dimensional structural frameworks like one-dimensional chains and two-dimensional layers.[22–30]

In order to solve the problem of exceedingly small birefringence, several feasible strategies are to regulate the non-π-conjugated optical active motifs by introducing functional metal cations to form polar metal-centered polyhedra,[31–34] and eventually synthesizing inventive types of large birefringence NLO crystals with the well-oriented arrangement: (i) the regulation of d^0-transition-metal cations (Ti^{4+}, Ta^{5+}, Mo^{6+}, Nb^{5+}, *etc.*) includes related examples, such as $ATiOPO_4$ (A = K, Rb) (Δn = 0.0921, 0.0884 at 1064 nm),[35,36] $Na_3TaP_2O_9$ (Δn = 0.1101),[37] $K_2ZnMoP_2O_{10}$ (Δn = 0.0534 at 450 nm),[38] $Na_{12}(NbO)_3(PO_4)_7$ (Δn = 0.03);[39] (ii) the moderation of stereochemical active lone pair cations (*e.g.*, Pb^{2+}, Bi^{3+}, Sb^{3+}, Sn^{2+}), for instance, $A_3PbBi(P_2O_7)_2$ (A = Rb, Cs) (Δn = 0.031, 0.020 at 1064 nm),[40] $A_3BaBi(P_2O_7)_2$ (A = Rb, Cs) (Δn = 0.025, 0.025 at 1064 nm),[41] $A_2Sb(P_2O_7)F$ (A = K, Rb) (Δn = 0.157, 0.150 at 546 nm),[42,43] Sn_2PO_4Cl (Δn = 0.162 at 546 nm);[44] (iii) the adjustment of highly polarizable d^{10} transition metals (Cd^{2+},

[a]China-Australia Joint Research Center for Functional Molecular Materials, School of Chemical Science and Engineering, Tongji University, Shanghai 200092, China. E-mail: chizhang@tongji.edu.cn, wuc@tongji.edu.cn
[b]Technical Institute of Physics and Chemistry, Chinese Academy of Sciences, Beijing 100190, China
[c]Research School of Chemistry, Australian National University, Canberra, Australian Capital Territory 2601, Australia
[d]Department of Chemistry, Graduate School of Science and Research Center for Materials Science, Nagoya University, Furo-Cho, Chikusa-ku, Nagoya 464-8602, Japan

†Electronic supplementary information (ESI) available: Details of crystallographic data, measurements of physical properties, and theoretical calculations. CCDC 2252377 and 2252378. For ESI and crystallographic data in CIF or other electronic format see DOI: https://doi.org/10.1039/d4qi02245a

‡These authors contributed equally to this work.

Published on 22 Oktober 2024. Downloaded on 14.10.25 16:33:10.

Zn^{2+}, Hg^{2+}, *etc.*), namely β-$Cd(PO_3)_2$ (Δn = 0.059 at 1064 nm),[1] $(NH_4)_3(H_3O)Zn_4(PO_4)_4$ (Δn = 0.032 at 1064 nm),[45] $LiHgPO_4$ (Δn = 0.068 at 1064 nm).[46] In addition, the "zipper" arrangements of the $[PO_4]$ motifs are building blocks that can lead to the enhancement of birefringence of the phosphate materials, for example, α-$YSc(PO_4)_2$ (Δn = 0.102 at 1064 nm).[47] However, the introduction of metal cations with d–d and f–f orbital interactions in non-π-conjugated motifs (*i.e.*, phosphates) may lead to a red-shift ultraviolet (UV) cut-off edge (λ_{cutoff}) of the compound, which has been observed in KTP (λ_{cutoff} = 350 nm).[48] Therefore, it is imperative to explore new short-wavelength UV NLO materials with excellent linear optical properties and develop innovative strategies for them.

π-Conjugated planar motifs with strong covalent bonds and p_π–p_π interactions provide a good platform for the development of UV NLO materials with superior optical properties.[49–54] Our previous studies have shown that the $[C(NH_2)_3]^+$ motif offers tremendous possibilities for the manipulation of optical properties. The resultant crystal $[C(NH_2)_3]_6(PO_4)_2{\cdot}3H_2O$ simultaneously displays short λ_{cutoff}, moderate birefringence, and strong SHG response.[55] In this work, two UV phosphate materials with pseudo 2D intercalated layers were successfully synthesized by employing the planar and tetrahedral motifs. Due to the different arrangement of planar and tetrahedral motifs within the pseudo 2D intercalated layers, the centrosymmetric (CS) 1-methylimidazolium phosphate $(C_4H_7N_2)(H_2PO_4)$ was varied into the noncentrosymmetric (NCS) imidazolium phosphate $(C_3H_5N_2)(H_2PO_4)$. Compared with the typical π-conjugated motifs ($(BO_3)^{3-}$, $(CO_3)^{2-}$, and $(NO_3)^-$), the $(C_3H_5N_2)^+$ motif exhibits greater hyperpolarizability, wider highest occupied molecular orbital–lowest unoccupied molecular orbital (HOMO–LUMO) gap, and larger polarizability anisotropy, indicating that the planar $(C_3H_5N_2)^+$ motifs serve as a novel optical active building block in the design of UV NLO materials (Fig. 1). Therefore, the $(C_3H_5N_2)(H_2PO_4)$ exhibits large birefringence (Δn = 0.15 at 546 nm), wide optical band gap (5.41 eV), and phase-matching SHG response (0.1 × KDP at 1064 nm). The theoretical calculation of $(C_3H_5N_2)(H_2PO_4)$ shows that the optical anisotropy related to birefringence is dominated by the planar $(C_3H_5N_2)^+$ motifs within pseudo 2D intercalated $^2_\infty[(C_3H_5N_2)(H_2PO_4)]$ layer, and the optical band gap is contributed by the synergistic effect of planar $(C_3H_5N_2)^+$ and tetrahedral $(H_2PO_4)^-$ motifs.

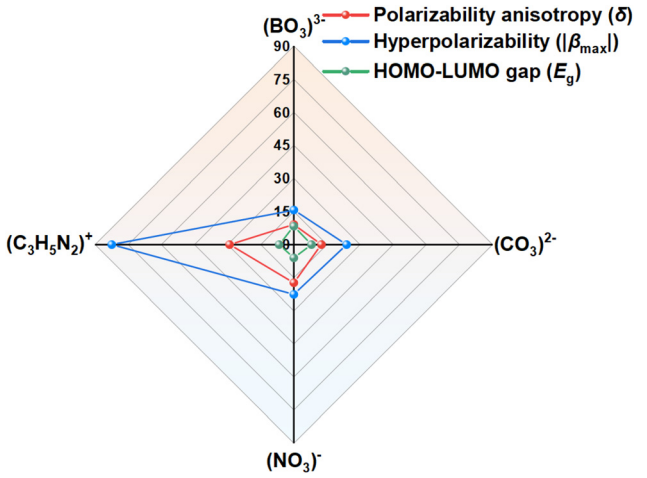

Fig. 1 Polarizability anisotropies, hyperpolarizabilities, and HOMO–LUMO gaps for typical π-conjugated functional motifs and the $(C_3H_5N_2)^+$ cation.

2. Experimental section

2.1 Reagents

The reagents operated in this work were purchased commercially without any further purification: phosphoric acid (H_3PO_4, Tansoole Chemical Reagent, 85 wt% in H_2O solution), imidazole ($C_3H_4N_2$, Tansoole Chemical Reagent, 95%), and 1-methylimidazole ($C_4H_6N_2$, Energy Chemical Reagent, 95%).

2.2 Synthesis of $(C_4H_7N_2)(H_2PO_4)$

The stoichiometric materials of $C_4H_6N_2$ (729 μL, 10.0 mmol) and H_3PO_4 (538 μL, 10.0 mmol) combined with deionized water (10.0 mL) were stirred and transferred into a 20 ml beaker. After 14 days, colorless block-shaped $(C_4H_7N_2)(H_2PO_4)$ crystals were obtained by utilizing the slow evaporation method in a clean fume hood with a yield of 80% (based on P) (Fig. S1†).

2.3 Synthesis of $(C_3H_5N_2)(H_2PO_4)$

A similar procedure was followed for the synthesis of colorless plate-shaped $(C_3H_5N_2)(H_2PO_4)$ crystals mixed in a molar ratio of 1 : 1 of $C_3H_4N_2$ (0.681 g, 10.0 mmol) and H_3PO_4 (538 μL, 10.0 mmol) with deionized water (10.0 mL) in a yield higher than 86% (based on P). The $(C_3H_5N_2)(H_2PO_4)$ crystals were exposed at room temperature conditions for more than 3 months without any decomposition (Fig. S1†).

2.4 Single crystal X-ray diffraction

The single crystal X-ray diffraction data from high quality $(C_4H_7N_2)(H_2PO_4)$ and $(C_3H_5N_2)(H_2PO_4)$ crystals were collected through a Bruker D8 VENTURE CMOS X-ray source equipped with graphite-monochromatic Mo-Kα radiation (λ = 0.71073 Å) at 293(2) K. APEX III software was executed to deal with the data collection and reduction. The absorption correction was performed using a multiscan-type method. The structures of $(C_4H_7N_2)(H_2PO_4)$ and $(C_3H_5N_2)(H_2PO_4)$ crystals were solved by direct methods, which were refined on F^2 by full-matrix least-squares methods *via* the OLEX2 software package.[56–58] Anisotropic displacement parameters were applied to refine all atoms other than hydrogen. Based on the PLATON program, none of the possible higher symmetry was found in the absolute structures.[59] The crystallographic data of $(C_4H_7N_2)(H_2PO_4)$ and $(C_3H_5N_2)(H_2PO_4)$ are listed in Table 1. More detailed crystallographic data are shown in Tables S1–S5,† including the selected bond distances (Å) and angles (°), atomic coordinates

 This journal is © the Partner Organisations 2024

Published on 22 Oktober 2024. Downloaded on 14.10.25 16:33:10.

Table 1 Crystallographic data and refinement details for $(C_4H_7N_2)(H_2PO_4)$ and $(C_3H_5N_2)(H_2PO_4)$

Formula	$(C_4H_7N_2)(H_2PO_4)$	$(C_3H_5N_2)(H_2PO_4)$
Formula weight	180.10	166.08
Temperature (K)	297(0) K	279(0) K
Crystal system	Monoclinic	Orthorhombic
Space group	$P2_1/n$ (no. 14)	$Pna2_1$ (no. 33)
a (Å)	8.1708(5)	8.3021(6)
b (Å)	9.9677(6)	17.5648(12)
c (Å)	9.8120(5)	4.7203(3)
α (°)	90	90
β (°)	95.695(2)	90
γ (°)	90	90
V (Å^3)	795.18(8)	688.34(8)
Z	4	4
$\rho_{calc.}$ (g cm^{-3})	1.504	1.603
μ (mm^{-1})	0.317	0.359
F (000)	376	344
θ (°)	2.92–27.10	2.71–27.86
Limiting indices	$-10 \le h \le 10$, $-12 \le k \le 12$, $-12 \le l \le 12$	$-10 \le h \le 10$, $-20 \le k \le 23$, $-6 \le l \le 5$
R_{int}	0.048	0.0213
Reflections collected/unique	9014/1758	4216/1549
Goodness of fit on F^2	1.046	1.083
R_1, wR_2 $[I > 2\sigma(I)]^a$	0.0480/0.0974	0.0256/0.0668
R_1, wR_2 (all data)	0.0756/0.1111	0.0287/0.0697
Largest difference peak and hole (e Å^{-3})	0.23 and −0.33	0.19 and −0.25

^{a} $R_1 = \sum||F_o| - |F_c||/\sum|F_o|$; w$R_2 = [\sum w(F_o{}^2 - F_c{}^2)^2]/[\sum w(F_o{}^2)^2]^{1/2}$.

equivalent isotropic displacement parameters, hydrogen bond, and π–π stacking interactions.

2.5 Powder X-ray diffraction

Powder X-ray diffraction for $(C_4H_7N_2)(H_2PO_4)$ and $(C_3H_5N_2)(H_2PO_4)$ crystals were analyzed by a Bruker D8 X-ray diffractometer installed with Cu-Kα radiation (λ = 1.5418 Å). The scanning was conducted with the 2θ from 5 to 70° and a scan step width of 0.02°. The peak positions of $(C_4H_7N_2)(H_2PO_4)$ and $(C_3H_5N_2)(H_2PO_4)$ determined by the powder X-ray diffraction patterns are consistent with those simulated from CIF data obtained by single crystal X-ray diffraction (Fig. S2†), indicating the pure phases of two compounds.

2.6 Infrared (IR) spectroscopy

IR spectra of $(C_4H_7N_2)(H_2PO_4)$ and $(C_3H_5N_2)(H_2PO_4)$ compounds were measured with a Nicolet iS10 Fourier transform IR spectrometer, with a wavenumber range of 400–4000 cm^{-1} and a resolution of 4 cm^{-1}. The measured samples were prepared by mixing crystalline samples $(C_4H_7N_2)(H_2PO_4)$ and $(C_3H_5N_2)(H_2PO_4)$ with KBr, respectively, with a mass ratio of about 1 : 100.

2.7 UV-Vis-NIR diffuse reflectance and transmittance spectra

The UV-Vis-NIR diffuse reflectance spectra of $(C_4H_7N_2)(H_2PO_4)$ and $(C_3H_5N_2)(H_2PO_4)$ crystalline powders and the UV-Vis-NIR transmittance spectra of $(C_4H_7N_2)(H_2PO_4)$ and $(C_3H_5N_2)(H_2PO_4)$ crystals were recorded at ambient temperature. Data of their UV-Vis-NIR reflectance spectra and UV transmittance spectra were collected on a Cary 5000 UV-Vis-NIR spectrophotometer scanning in the range 200–1500 nm and 200–400 nm, respectively.

2.8 Thermal analysis

The thermogravimetric properties of $(C_4H_7N_2)(H_2PO_4)$ and $(C_3H_5N_2)(H_2PO_4)$ were tested using a Netzsch STA 409PC thermal analyzer. The two compounds were heated from room temperature to 600 °C with a rate of 15 °C min^{-1} under a nitrogen atmosphere after putting powder samples into platinum crucibles.

2.9 Second-order NLO measurements

Powder second harmonic generation (SHG) of $(C_3H_5N_2)(H_2PO_4)$ was tested by the Kurtz–Perry method using a Q-switched Nd:YAG laser with 1064 nm.[60] Crystalline $(C_3H_5N_2)(H_2PO_4)$ were sieved into the following five particle sizes (50–74, 74–105, 105–150, 150–200 and 200–280 μm) because SHG efficiency is influenced by the crystal particle size. Crystals KDP with the same particle size ranges were used as the benchmark.

2.10 Birefringence measurements

The birefringence of $(C_4H_7N_2)(H_2PO_4)$ and $(C_3H_5N_2)(H_2PO_4)$ were assessed by a ZEISS Axio Scope 5 polarizing microscope equipped with a Berek compensator under a 546 nm light source. The birefringence was determined according to the function: ΔR (retardation) = $|N_e - N_o| \times T = \Delta n \times T$. The optical path difference is ΔR, the measured birefringence is Δn, and the crystal thickness denotes T. The relative retardation was provided the positive and negative rotation of compensation.[61,62] The thicknesses of crystalline samples $(C_4H_7N_2)(H_2PO_4)$ and $(C_3H_5N_2)(H_2PO_4)$ were measure on a Bruker D8 VENTURE diffractometer.

2.11 Theoretical calculations

The first-principles calculations based on pseudopotential density functional theory (DFT)[63,64] methods of the NCS compound $(C_3H_5N_2)(H_2PO_4)$ were assessed by the CASTEP package.[65] Perdew, Burke, and Ernzerhof (PBE)[66] proposed the generalized gradient approximation (GGA) function[67] that was carried out to describe the correlation–exchange terms in the Hamiltonian. A kinetic energy cutoff of 489.80 eV and the Monkhorst–Pack k-point meshes[68] with a density of (2 × 1 × 4) points were opted in the Brillouin zone. The electronic structure of $(C_3H_5N_2)(H_2PO_4)$ was calculated from the experimentally obtained crystal structures, and its optical properties were calculated by the scissors-corrected PBE method.[69] Accordingly, its real part was determined by the Kramers–Kronig transform[70,71] after the imaginary part of the dielectric function ε_2 was calculated. The refractive indices n and the birefringence Δn were consequently obtained. Under the restriction of Kleinman's symmetry,[72] the static and dynamic second-order nonlinear susceptibilities χ^{abc} $(-2\omega, \omega, \omega)$ were employed the length-gauge formalism.[73,74] In the SHG-

Published on 22 Oktober 2024. Downloaded on 14.10.25 16:33:10.

weighted electron cloud calculations, the probability densities of all occupied (valence) or unoccupied (conduction) states projected onto real space are multiplied by a weighting factor that is related to the contribution to SHG efficiency, while the orbitals vital to SHG are intuitively highlighted in real space.[75] In real-space atom-cutting analysis, the contribution of each NLO-active motif to the SHG coefficient is obtained by excluding the wave functions in a sphere with a radius encompassing all atoms except the focused unit, that is, $\chi^2(A) = \chi^2$ (all atoms excluded except the focused unit).[76] With the assistance of Gaussian16 software,[77] the electronic structure properties of the asymmetric units of crystals and $(C_3H_5N_2)^+$ cation at the molecular level were obtained by using the DFT calculation of B3LYP/6-31G method.

3. Results and discussion

3.1 Crystal structure of $(C_4H_7N_2)(H_2PO_4)$

The CS compound $(C_4H_7N_2)(H_2PO_4)$ crystallizes in the monoclinic space group $P2_1/n$ (no. 14) with cell parameters of a = 8.1708(5) Å, b = 9.9677(6) Å, c = 9.8120(5) Å, β = 95.695(2) Å, and V = 795.18(8) Å^3 (Table 1). The asymmetric unit of $(C_4H_7N_2)(H_2PO_4)$ is composed of the positive-valence 1-methylimidazolium planar cation $(C_4H_7N_2)^+$ and the negative-valence tetrahedral dihydrogen phosphate anion $(H_2PO_4)^-$, which are joined by the hydrogen bond N_2–H_2···O_4 (Fig. 2a). The $(H_2PO_4)^-$ anions are connected to each other through the O_1–H_1···O_3 and O_2–H_{2B}···O_4 hydrogen bonds and form a one-dimensional (1D) inverse $^1_\infty[H_2PO_4]$ chain (Fig. 2b). The distance between two adjacent $^1_\infty[H_2PO_4]$ chains is 9.76 Å, in which the planar $(C_4H_7N_2)^+$ motifs are incorporated and are fixed by the N_2–H_2···O_4 and C_4–H_4···O_3 hydrogen bonds, and the planar $(C_4H_7N_2)^+$ motifs are alternately antiparallel, where the distance between the centroids of the cations along the a-axis direction is 3.68 Å and 4.63 Å (Table S5†). The pseudo 2D intercalated layer of the crystal $(C_4H_7N_2)(H_2PO_4)$ is formed by inverse $^1_\infty[H_2PO_4]$ chains and planar $(C_4H_7N_2)^+$ motifs (Fig. 2c). The 3D crystal structure of the compound $(C_4H_7N_2)(H_2PO_4)$ is stacked by pseudo 2D intercalated layers in an –AA′– mode, as well as interlayer hydrogen bonds, namely C_3–H_3···O_1 (Fig. 2d).

3.2 Crystal structure of $(C_3H_5N_2)(H_2PO_4)$

The NCS compound $(C_3H_5N_2)(H_2PO_4)$ converges to polar orthorhombic space group $Pna2_1$ (no. 33), which contains cell parameters of a = 8.3021(6) Å, b = 17.5648(12) Å, c = 4.7203(3) Å, and V = 688.34(8) Å^3 (Table 1). The asymmetric unit of $(C_3H_5N_2)(H_2PO_4)$ contains the positive-valence imidazolium planar cation $(C_3H_5N_2)^+$ and the negative-valence tetrahedral dihydrogen phosphate anion $(H_2PO_4)^-$, which are interconnected by hydrogen bond N_2–H_2···O_1 (Fig. 2e). The (H_2PO_4) tetrahedron possesses P–O bonds in the range of 1.5043(15)–1.5739(18) Å, and the tetrahedra are linked by the O_2–H_{2B}···O_3 hydrogen bonds along the c-axis to build a uniform $^1_\infty[H_2PO_4]$ chain (Fig. 2f). The distance between adjacent $^1_\infty[H_2PO_4]$ chains is 8.78 Å, in which the planar $(C_3H_5N_2)^+$ motifs are introduced and are firmly fastened through hydrogen bonds (*i.e.*, C_1–H_{1A}···O_4, C_2–H_{2A}···O_2, and N_2–H_2···O_1), and the planar cations are aligned in a uniform manner, where the distance between the centroids of adjacent cations is 4.72 Å (Table S5†). The pseudo 2D alternating intercalated layer is constructed by uniform $^1_\infty[H_2PO_4]$ chains and the planar $(C_3H_5N_2)^+$ motifs in the bc plane (Fig. 2g). The resultant 3D framework is packed by pseudo 2D intercalated layers in a –BB′– pattern, and two kinds of hydrogen bonds between layers, namely N_1–H_1···O_1 and O_4–H_4···O_3 (Fig. 2h).

3.3 CS $(C_4H_7N_2)(H_2PO_4)$ *vs.* NCS $(C_3H_5N_2)(H_2PO_4)$ structures

Compounds $(C_4H_7N_2)(H_2PO_4)$ and $(C_3H_5N_2)(H_2PO_4)$ have similar structural skeletons, which are 3D crystal frameworks constructed by pseudo 2D intercalated structures with $^1_\infty[H_2PO_4]$ chain arrangements and planar motif introduction. The difference between the structures of compounds $(C_4H_7N_2)(H_2PO_4)$ and $(C_3H_5N_2)(H_2PO_4)$ is the arrangement of $^1_\infty[H_2PO_4]$ chains, which is attributed to the different hydrogen bonding

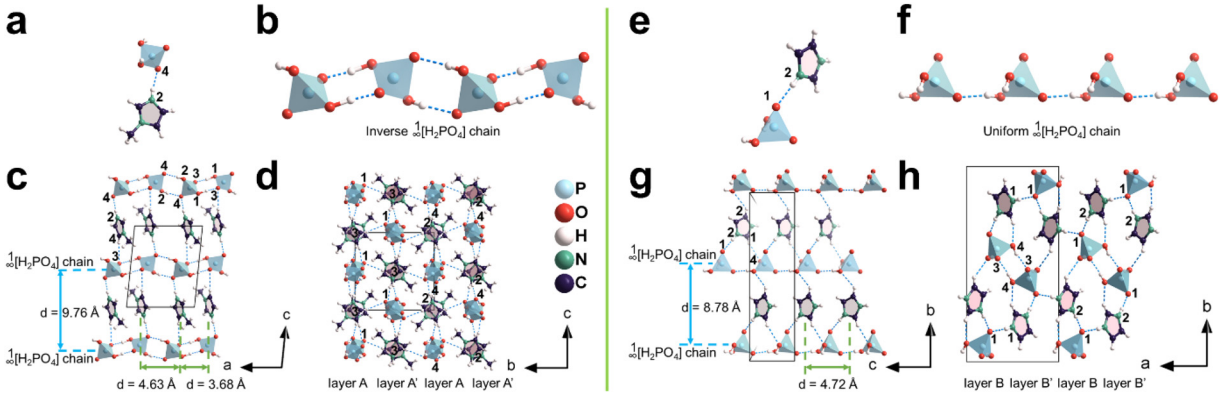

Fig. 2 Diagrams of $(C_4H_7N_2)(H_2PO_4)$ structure: (a) asymmetric unit. (b) Inverse $^1_\infty[H_2PO_4]$ chain. (c) Pseudo 2D intercalated structure in the ac plane. (d) 3D structure viewed in the bc plane. Diagrams of $(C_3H_5N_2)(H_2PO_4)$ structure: (e) asymmetric unit. (f) Uniform $^1_\infty[H_2PO_4]$ chain. (g) Pseudo 2D intercalated structure in the bc plane. (h) 3D structure viewed in the ab plane.

 This journal is © the Partner Organisations 2024

Published on 22 Oktober 2024. Downloaded on 14.10.25 16:33:10.

interactions between the $(H_2PO_4)^-$ motifs within the $^1_\infty[H_2PO_4]$ chains. In compound $(C_4H_7N_2)(H_2PO_4)$, the adjacent $(H_2PO_4)^-$ motifs are connected by double hydrogen bonds, forming an inverse $^1_\infty[H_2PO_4]$ chain (Fig. 2b); while in compound $(C_3H_5N_2)(H_2PO_4)$, the adjacent $(H_2PO_4)^-$ motifs are connected by single hydrogen bond, forming a uniform $^1_\infty[H_2PO_4]$ chain (Fig. 2f). In compound $(C_4H_7N_2)(H_2PO_4)$, the $^1_\infty[H_2PO_4]$ chains are arranged in reverse order, so the planar $(C_4H_7N_2)^+$ motifs are distributed on both sides of the $^1_\infty[H_2PO_4]$ chain through hydrogen bonds (Fig. 3a). When the $^1_\infty[H_2PO_4]$ chains are assembled into a pseudo 2D intercalated layer, the planar $(C_4H_7N_2)^+$ motifs in the adjacent $^1_\infty[H_2PO_4]$ chains are antiparallelly arranged, and the distance between the centroids of the adjacent planar $(C_4H_7N_2)^+$ motifs is 3.68 Å. This indicates that the planar $(C_4H_7N_2)^+$ motifs exhibit a slight parallel displacement in π–π stacking, and the π–π interactions between them are extremely strong (Fig. 3b). The π–π stacking of the antiparallel pairing mode naturally enhances the giant dipole–dipole interaction, which results in a deleterious CS structure. The result is that the dipole–dipole interactions between the adjacent $(C_4H_7N_2)^+$ cations in the compound $(C_4H_7N_2)(H_2PO_4)$ are strong enough to fall into the center-symmetry trap. In compound $(C_3H_5N_2)(H_2PO_4)$, the $^1_\infty[H_2PO_4]$ chains are arranged uniformly, so the planar $(C_3H_5N_2)^+$ motifs are only distributed on one side of the $^1_\infty[H_2PO_4]$ chain through hydrogen bonds (Fig. 3c). When the $^1_\infty[H_2PO_4]$ chains are assembled into a pseudo 2D intercalated layer, the planar $(C_3H_5N_2)^+$ motifs in the adjacent $^1_\infty[H_2PO_4]$ chains are uniformly arranged. The distance between the centroids of the adjacent planar $(C_3H_5N_2)^+$ motifs is 4.72 Å, indicating that the $(C_3H_5N_2)^+$ cations are in a completely parallel-displaced π–π stacking arrangement and the π–π stacking interaction between them can be ignored (Fig. 3d). Since the distance of the planar $(C_3H_5N_2)^+$ motifs is far away, no dipole–dipole interaction between the planar $(C_3H_5N_2)^+$ motifs is observed in the $(C_3H_5N_2)(H_2PO_4)$ structure, which breaks the central symmetry and successfully forms a NCS and polar crystal structure. In addition, all pseudo 2D intercalated layers in the compounds $(C_4H_7N_2)(H_2PO_4)$ and $(C_3H_5N_2)(H_2PO_4)$ are approximately parallel in the opposite direction. Therefore, the pseudo 2D intercalated layer will enhance the optical anisotropy of these two compounds, which can be verified in subsequent tests.

3.4 IR spectra

The infrared vibration frequencies of $(C_4H_7N_2)(H_2PO_4)$ and $(C_3H_5N_2)(H_2PO_4)$ are shown in Fig. S3.† The O–P–O bending vibration at 500–550 cm^{-1}, the P–O asymmetric stretching vibration at 945/949 cm^{-1}, the P–O symmetric stretching vibration at 1057/1088 cm^{-1}, and the O–H stretching vibration at 3138/3135 cm^{-1} are ascribed to the characteristic frequencies of the tetrahedral $(H_2PO_4)^-$ anions of $(C_4H_7N_2)(H_2PO_4)$ and $(C_3H_5N_2)(H_2PO_4)$, respectively. The C–H stretching vibration at 3084 cm^{-1} and stretching vibration at 1587, 1552 and 1471 cm^{-1} of the 1-methylimidazolium skeleton, methyl C–H stretching vibration at 2962 and 2872 cm^{-1}, corresponding to the absorption peak of $(C_4H_7N_2)^+$ cations in $(C_4H_7N_2)(H_2PO_4)$. The vibration absorption peaks of $(C_3H_5N_2)^+$ cations in $(C_3H_5N_2)(H_2PO_4)$ contain the N–H stretching

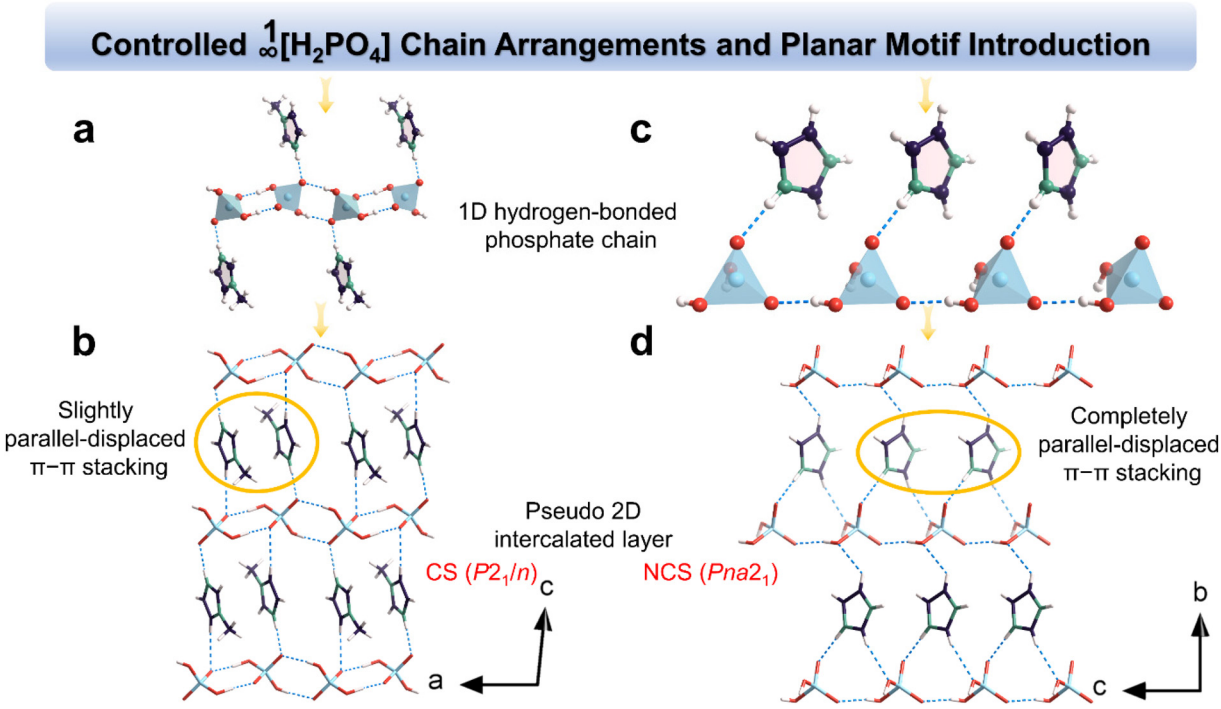

Fig. 3 The structural design based on controlled $^1_\infty[H_2PO_4]$ chain arrangements and planar motif introduction. The distribution of the planar motifs connected with the $^1_\infty[H_2PO_4]$ chain (a and c) and pseudo 2D intercalated layers (b and d) in the CS $(C_4H_7N_2)(H_2PO_4)$ and NCS $(C_3H_5N_2)(H_2PO_4)$.

Published on 22 Oktober 2024. Downloaded on 14.10.25 16:33:10.

vibration at 3181 cm^{-1}, the C–H stretching vibration at 2971 cm^{-1}, and the skeleton stretching vibration of imidazole at 1597 and 1467 cm^{-1}. In addition, the IR peaks at around 2330 cm^{-1} are attributed to hydrogen bonds between $(H_2PO_4)^-$ anions,[78] while the IR peak at 2600–2800 cm^{-1} belongs to hydrogen bonds between planar cations and $(H_2PO_4)^-$ anions.[79] The assignment of these peaks agrees well with the compounds $(C_4H_7N_2)(H_2PO_4)$ and $(C_3H_5N_2)(H_2PO_4)$.

3.5 UV-Vis-NIR diffuse reflectance and transmittance spectra

The UV-Vis-NIR diffuse reflectance spectra indicate that the optical band gaps of $(C_4H_7N_2)(H_2PO_4)$ and $(C_3H_5N_2)(H_2PO_4)$ crystalline powders are 5.08 eV and 5.13 eV, respectively (Fig. S4a and b†), according to the Kubelka–Munk formula $F(R) = (1 - R)^2/(2R)$.[80,81] To determine the accurate optical band gap,[82] we also performed UV transmittance measurements on unpolished single crystals of $(C_4H_7N_2)(H_2PO_4)$ and $(C_3H_5N_2)(H_2PO_4)$, yielding UV cutoff edges at 238 nm and 229 nm (Fig. 4a and b), corresponding to band gaps of 5.21 eV and 5.41 eV, respectively. Interestingly, the UV cut-off edge of $(C_3H_5N_2)(H_2PO_4)$ is blue-shifted, which is related to the conjugated effect of different planar motifs. The hyperconjugative effect is observed in $(C_4H_7N_2)(H_2PO_4)$ because the C–H bond electrons in the methyl group overlap with the π electrons of the conjugated imidazolium motif, which consequently increases the extent of electron delocalization and induces a red-shift in the UV cut-off edge. In comparison, there is no hyperconjugative effect in $(C_3H_5N_2)(H_2PO_4)$, which leads to a blue shift in the UV cut-off edge. The λ_{cutoff} of $(C_3H_5N_2)(H_2PO_4)$ is shorter than aromatic heterocyclic compounds, such as $(C_4H_6N_3)(H_2PO_3)$ (λ_{cutoff} = 346 nm),[51] $(C_5H_6ON)(H_2PO_4)$ (λ_{cutoff} = 264 nm),[50] and $(H_2N)_2CNH(CH_2)_3CH(NH_3)COO{\cdot}H_2PO_4{\cdot}H_2O$ (λ_{cutoff} = 230 nm).[83]

3.6 Thermal stabilities

Fig. S5† shows the results of the thermogravimetric analysis under a nitrogen atmosphere. Compounds $(C_4H_7N_2)(H_2PO_4)$ and $(C_3H_5N_2)(H_2PO_4)$ were stable up to 76 °C and 68 °C, respectively.

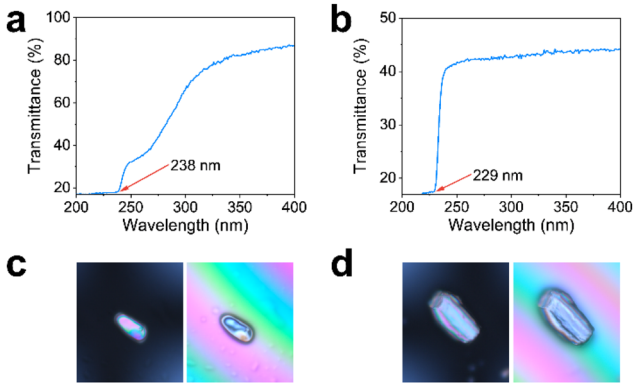

Fig. 4 UV transmittance spectra of $(C_4H_7N_2)(H_2PO_4)$ (a) and $(C_3H_5N_2)(H_2PO_4)$ (b). A comparison between the original crystal and the crystal achieving complete extinction of $(C_4H_7N_2)(H_2PO_4)$ (c) and $(C_3H_5N_2)(H_2PO_4)$ (d).

3.7 SHG response

The prerequisite for generating SHG is that the crystal possesses a NCS structure, so the crystalline samples $(C_3H_5N_2)(H_2PO_4)$ are measured at a wavelength of 1064 nm based on the Kurtz–Perry method. The SHG intensity of $(C_3H_5N_2)(H_2PO_4)$ increases with the increase of particle size, indicating phase-matching (PM) at 1064 nm (Fig. S6a†). The SHG signal of $(C_3H_5N_2)(H_2PO_4)$ is estimated to be approximately 0.1 × KDP in a particle size range of 105–150 μm (Fig. S6b†). The reason for the weak SHG response is that the adjacent pseudo 2D intercalated layers tend to be antiparallel.

3.8 Birefringence

The birefringences of $(C_4H_7N_2)(H_2PO_4)$ and $(C_3H_5N_2)(H_2PO_4)$ were measured by a ZEISS Axio 5 polarizing microscope at 546 nm. In Fig. 4c and d, two compounds have completely extinguished, and the experimental retardations were 1.67 μm and 1.98 μm, respectively. The corresponding thicknesses of the two crystals are 14.0 μm and 13.6 μm for $(C_4H_7N_2)(H_2PO_4)$ and $(C_3H_5N_2)(H_2PO_4)$, respectively (Fig. S7†). According to the equation ΔR (retardation) = $\Delta n \times T$, the birefringences are 0.12 and 0.15 for $(C_4H_7N_2)(H_2PO_4)$ and $(C_3H_5N_2)(H_2PO_4)$, respectively. The birefringences of $(C_4H_7N_2)(H_2PO_4)$ and $(C_3H_5N_2)(H_2PO_4)$ are much larger than that of other compounds containing phosphate motifs (Table S6†), such as $BaP_3O_{10}Cl$ (Δn = 0.028 at 1064 nm),[16] $NaNH_4PO_3F{\cdot}H_2O$ (Δn = 0.053 at 589.3 nm),[84] $LiCs_2PO_4$ (Δn = 0.01 at 1064 nm),[85] and $[C(NH_2)_3]_6(PO_4)_2{\cdot}3H_2O$ (Δn = 0.078 at 546 nm).[55] The π-conjugated planar motifs have large polarizability anisotropy due to the π-electrons delocalization, while non-conjugated phosphate tetrahedrons have small polarizability anisotropy due to high geometric symmetry. The birefringence of $(C_4H_7N_2)(H_2PO_4)$ and $(C_3H_5N_2)(H_2PO_4)$ mainly stems from planar $(C_4H_7N_2)^+$ and $(C_3H_5N_2)^+$ motifs. In addition, the pseudo 2D intercalated layers and the antiparallel mode between the pseudo 2D intercalated layers are also conducive to large optical anisotropy, resulting in large birefringence.

3.9 Theoretical studies

The electronic structure of $(C_3H_5N_2)(H_2PO_4)$ was theoretically calculated to bring the relationship between crystal structure and optical properties to light. As displayed in Fig. 5a, $(C_3H_5N_2)(H_2PO_4)$ is an indirect band gap material with a band gap of 3.685 eV, which is smaller than the experimental value (5.41 eV) due to the approximation problem of the exchange-correlation function.[86] The corresponding total and partial density of states (TDOS and PDOS) reveal that the O-2p of the tetrahedral $(H_2PO_4)^-$ motifs makes the primary contributions to the top of the valence band (VB) (Fig. 5b). The bottom of the conduction band (CB) predominantly originates from the C-2p and N-2p of the planar $(C_3H_5N_2)^+$ motifs. These results indicate that the band gap of $(C_3H_5N_2)(H_2PO_4)$ is determined by the $(C_3H_5N_2)^+$ and the $(H_2PO_4)^-$ motifs.

 This journal is © the Partner Organisations 2024

Published on 22 Oktober 2024. Downloaded on 14.10.25 16:33:10.

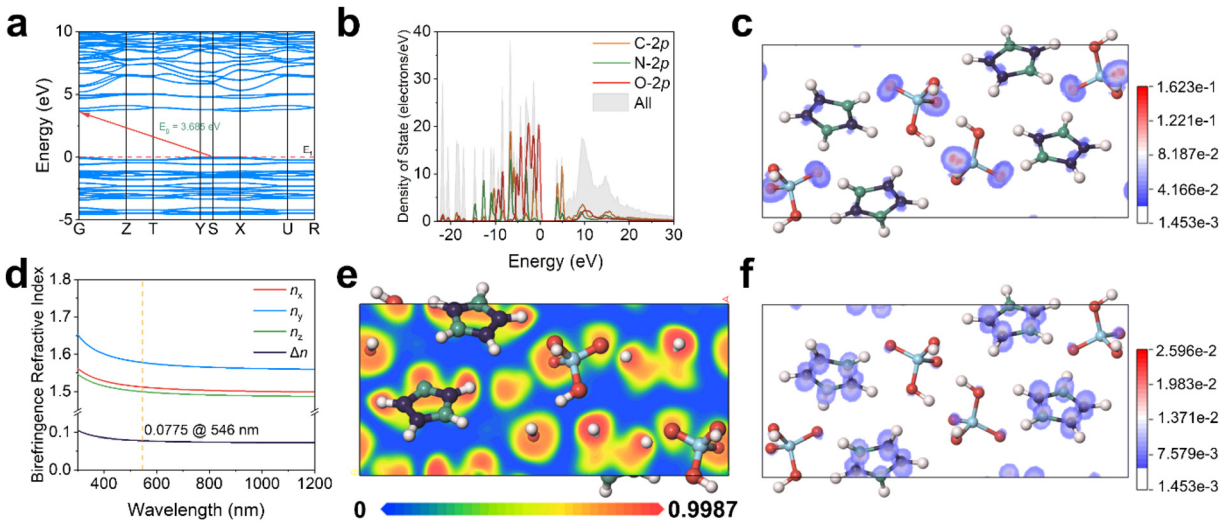

Fig. 5 Theoretical calculations of $(C_3H_5N_2)(H_2PO_4)$: (a) the calculated band gap. (b) The total and partial densities of states. The SHG weight electron density in the occupied state (c) and unoccupied state (f). (d) The calculated dispersion of refractive index curve and birefringence (Δn). (e) c-Axis projection of the electron localization function (ELF). The Fermi level (E_F) is marked.

Since $(C_3H_5N_2)(H_2PO_4)$ crystallizes in the polar space group $Pna2_1$, it has three non-zero independent SHG coefficients (d_{15}, d_{24}, and d_{33}) under the Kleinman symmetry restriction (Table S7†). The calculated effective SHG coefficient (d_{eff}) value of the $(C_3H_5N_2)(H_2PO_4)$ is 0.11 pm V^{-1} under 1064 nm irradiation (d_{eff} (KDP) = 0.39 pm V^{-1}),[85] which is close to the experimental measurement value. To evaluate qualitatively the contribution of each component to the SHG response, SHG weight electron density analysis was performed on $(C_3H_5N_2)(H_2PO_4)$. The SHG weight density of the occupied state mainly comes from the O-2p non-bonding orbital from the tetrahedral $(H_2PO_4)^-$ motifs and is slightly derived from the C-2p π-bonding orbital of planar $(C_3H_5N_2)^+$ motifs (Fig. 5c), while the SHG weight density of the unoccupied state mainly comes from the C-2p and N-2p π-antibonding orbitals from the planar $(C_3H_5N_2)^+$ motifs and is slightly derived from the O-2p antibonding orbital of tetrahedral $(H_2PO_4)^-$ motifs (Fig. 5f), respectively. At the same time, the real-space atomic cutting analysis was also carried out to quantify the contribution of $(C_3H_5N_2)^+$ and $(H_2PO_4)^-$ motifs to the SHG response (Table S7†). The SHG contribution percentages of $(C_3H_5N_2)^+$ (55.56%) and $(H_2PO_4)^-$ (44.44%) were calculated. Obviously, the planar and tetrahedral motifs have a synergistic effect on the SHG response for the $(C_3H_5N_2)(H_2PO_4)$ crystal. Compared with the $(H_2PO_4)^-$ motif, the $(C_3H_5N_2)^+$ motif plays a major role in the SHG coefficient. Unfortunately, the adjacent pseudo 2D intercalated layers in the $(C_3H_5N_2)(H_2PO_4)$ crystal are arranged in an almost antiparallel manner, resulting in a weak SHG response.

$(C_3H_5N_2)(H_2PO_4)$ is a positive biaxial crystal because the compound $(C_3H_5N_2)(H_2PO_4)$ belongs to the orthorhombic system and follows $n_y - n_x > n_x - n_z$. According to the wavelength-dependent refractive index curve, the calculated birefringence (Δn) of $(C_3H_5N_2)(H_2PO_4)$ is 0.078 at 546 nm (Fig. 5d). Obviously, the calculated birefringence (Δn_{cal} = 0.078 at 546 nm) is smaller than the experimental birefringence (Δn_{exp} = 0.15 at 546 nm). This may be due to the fact that the calculation of the refractive index is not strictly along a specific optical principal axis. Compared with those of KDP (Δn = 0.034 at 1064 nm)[36] and $(H_2N)_2CNH(CH_2)_3CH(NH_3)COO{\cdot}H_2PO_4{\cdot}H_2O$ (Δn = 0.075 at 1064 nm),[87] the large birefringence of $(C_3H_5N_2)(H_2PO_4)$ is attributed to the introduction of planar $(C_3H_5N_2)^+$ motifs, which possess a π-conjugated aromatic heterocyclic structure. A large overlap between the C-2p and N-2p orbitals is observed, leading to a strong p_π–p_π interaction that is beneficial for generating large polarizability anisotropy (Fig. 5e). In comparison with traditional π-conjugated planar motifs, $(C_3H_5N_2)^+$ motif shows large optical anisotropy, which is conducive to generating large birefringence. To better understand the origin of the optical anisotropy of $(C_3H_5N_2)(H_2PO_4)$, the real-space atomic cutting analysis (Table S7†) was also used. The contribution of the $(C_3H_5N_2)^+$ motif (78.08%) is about 3.56 times that of the $(H_2PO_4)^-$ motif (21.92%), indicating that planar $(C_3H_5N_2)^+$ motifs have an important contribution to birefringence. In addition, the pseudo 2D intercalated layers in the $(C_3H_5N_2)(H_2PO_4)$ crystal and the nearly antiparallel arrangement of adjacent pseudo 2D intercalated layers are conducive to optical anisotropy, resulting in large birefringence (Fig. 2g and h).

4. Conclusions

In brief, CS phosphate $(C_4H_7N_2)(H_2PO_4)$ and NCS phosphate $(C_3H_5N_2)(H_2PO_4)$ were successfully synthesized, in which planar and tetrahedral motifs were employed simultaneously to construct pseudo 2D intercalated layers with strong and negligible dipole–dipole interactions, respectively. The modulation

Published on 22 Oktober 2024. Downloaded on 14.10.25 16:33:10.

of the dipole–dipole interaction leads to the inversion and uniformity of the planar and tetrahedral motifs in CS and NCS phosphates, respectively. The NCS $(C_3H_5N_2)(H_2PO_4)$ possesses a wide band gap (5.41 eV), large birefringence (0.15 at 546 nm), and a phase-matching SHG response (0.1 × KDP). The first-principles calculations and structural analysis clarify that the uniform $^1_\infty[H_2PO_4]$ chains and planar $(C_3H_5N_2)^+$ motifs work together to form pseudo 2D intercalated layers, and the nearly antiparallel arrangement between adjacent pseudo 2D intercalated layers is conducive to large birefringence. Among the above optical performance contributions, planar $(C_3H_5N_2)^+$ motifs play a major role. In addition, the synergistic effect of the tetrahedral $(H_2PO_4)^-$ and planar $(C_3H_5N_2)^+$ motifs affects the optical band gap. This study offers new insight into obtaining optical anisotropy structures *via* pseudo 2D intercalated layer, and promotes the development of high-performance NCS materials.

Data availability

The authors confirm that the data supporting the findings of this study are available within the article and its ESI.†

Conflicts of interest

There are no conflicts to declare.

Acknowledgements

This research was financially supported by the National Natural Science Foundation of China (no. 51432006, and 52002276), the Ministry of Education of China for the Changjiang Innovation Research Team (no. IRT14R23), the Ministry of Education and the State Administration of Foreign Experts Affairs for the 111 Project (no. B13025), and the Innovation Program of Shanghai Municipal Education Commission. M. G. H. thanks the Australian Research Council for support (DP170100411). The authors thank Dr Wenyan Dan for his help in single-crystal structure determination.

References

1 J. R. Lv, Y. Y. Qian, Q. Jing, X. M. Wang, M. H. Lee and Z. H. Chen, Two Metal Phosphate Nonlinear Optical Materials Simultaneously Exhibiting Ultraviolet Transparence and a Large Birefringence, *Chem. Mater.*, 2022, **34**, 5919–5927.

2 L. Xiong, L. M. Wu and L. Chen, A General Principle for DUV NLO Materials: π-Conjugated Confinement Enlarges Band Gap, *Angew. Chem., Int. Ed.*, 2021, **60**, 25063–25067.

3 H. N. Liu, H. P. Wu, Z. G. Hu, J. Y. Wang, Y. C. Wu and H. W. Yu, $Cs_3[(BOP)_2(B_3O_7)_3]$: A Deep-Ultraviolet Nonlinear Optical Crystal Designed by Optimizing Matching of Cation and Anion Groups, *J. Am. Chem. Soc.*, 2023, **145**, 12691–12700.

4 M. Mutailipu, J. Han, Z. Li, F. M. Li, J. J. Li, F. F. Zhang, X. F. Long, Z. H. Yang and S. L. Pan, Achieving the full-wavelength phase-matching for efficient nonlinear optical frequency conversion in $C(NH_2)_3BF_4$, *Nat. Photonics*, 2023, **17**, 694–701.

5 H. T. Tian, C. S. Lin, Y. Q. Zhou, X. Zhao, H. X. Fan, T. Yan, N. Ye and M. Luo, Design of the Ionic Organic Nonlinear Optical Material $NH_4[LiC_3H(CH_3)O_4]$ with Ultrawide Band Gap and Moderate Birefringence, *Angew. Chem., Int. Ed.*, 2023, **62**, e202304858.

6 Y. L. Hu, C. Wu, X. X. Jiang, K. N. Duanmu, Z. P. Huang, Z. S. Lin, M. G. Humphrey and C. Zhang, Ultrashort Phase-Matching Wavelength and Strong Second-Harmonic Generation in Deep-UV-Transparent Oxyfluorides by Covalency Reduction, *Angew. Chem., Int. Ed.*, 2023, **62**, e202315133.

7 C. Wu, X. X. Jiang, Z. J. Wang, L. Lin, Z. S. Lin, Z. P. Huang, X. F. Long, M. G. Humphrey and C. Zhang, Giant Optical Anisotropy in the UV-Transparent 2D Nonlinear Optical Material $Sc(IO_3)_2(NO_3)$, *Angew. Chem., Int. Ed.*, 2021, **60**, 3464–3468.

8 H. Y. Sha, Y. R. Shang, Z. J. Wang, R. B. Su, C. He, X. M. Yang and X. F. Long, The Strategy to Improve the Phase Matching Ability in Tetrahedron-Based Deep-Ultraviolet Nonlinear Optical Crystals, *Adv. Opt. Mater.*, 2023, **11**, 2300987.

9 Y. G. Chen, X. W. Hu, Y. Guo, S. G. Zhao, B. B. Zhang, X. Zhang and X. M. Zhang, Edge-Sharing Tetrahedra Realizing Superior Birefringence and High Deep-Ultraviolet Transmittance in α-$Be_3(H_2O)_2(PO_4)_2$ Crystal Synthesized by Mild Chemistry, *Chem. Mater.*, 2024, **36**, 4775–4781.

10 L. Qi, X. X. Jiang, K. N. Duanmu, C. Wu, Z. S. Lin, Z. P. Huang, M. G. Humphrey and C. Zhang, Quadruple-Bidentate Nitrate-Ligated $A_2Hg(NO_3)_4$ (A = K, Rb): Strong Second-Harmonic Generation and Sufficient Birefringence, *Angew. Chem., Int. Ed.*, 2023, **62**, e202309365.

11 S. Liu, X. X. Jiang, L. Qi, Y. L. Hu, K. N. Duanmu, C. Wu, Z. S. Lin, Z. P. Huang, M. G. Humphrey and C. Zhang, An Unprecedented $[BO_2]$-Based Deep-Ultraviolet Transparent Nonlinear Optical Crystal by Superhalogen Substitution, *Angew. Chem., Int. Ed.*, 2024, **63**, e202403328.

12 T. H. Wu, X. X. Jiang, K. N. Duanmu, C. Wu, Z. S. Lin, Z. P. Huang, M. G. Humphrey and C. Zhang, Secondary-Bond-Driven Construction of a Polar Material Exhibiting Strong Broad-Spectrum Second-Harmonic Generation and Large Birefringence, *Angew. Chem., Int. Ed.*, 2024, **63**, e202318107.

13 F. Zernike, Refractive Indices of Ammonium Dihydrogen Phosphate and Potassium Dihydrogen Phosphate between 2000 Å and 1.5 μ, *J. Opt. Soc. Am.*, 1964, **54**, 1215–1220.

14 F. C. Zumsteg, J. D. Bierlein and T. E. Gier, $K_xRb_{1-x}TiOPO_4$: A new nonlinear optical material, *J. Appl. Phys.*, 1976, **47**, 4980–4985.

 This journal is © the Partner Organisations 2024

Published on 22 Oktober 2024. Downloaded on 14.10.25 16:33:10.

15 D. Xu, M. H. Jiang and Z. K. Tan, A new phase matchable nonlinear optic crystal L-arginine phosphate monohydrate, *Acta Chim. Sin.*, 1983, **41**, 570–573.
16 P. Yu, L. M. Wu, L. J. Zhou and L. Chen, Deep-Ultraviolet Nonlinear Optical Crystals: $Ba_3P_3O_{10}X$ (X = Cl, Br), *J. Am. Chem. Soc.*, 2014, **136**, 480–487.
17 Y. Q. Zhou, L. L. Cao, C. S. Lin, M. Luo, T. Yan, N. Ye and W. D. Cheng, $AMgPO_4{\cdot}6H_2O$ (A = Rb, Cs): strong SHG responses originated from orderly PO_4 groups, *J. Mater. Chem. C*, 2016, **4**, 9219–9226.
18 F. F. Yuan, L. Hu, Z. Y. Bai, L. H. Liu, Y. S. Huang, L. Z. Zhang, D. S. Wei and Z. B. Lin, Struvite-type $AMgPO_4{\cdot}6H_2O$ (A = NH_4, K): Two Natural Deep-Ultraviolet Transparent Nonlinear Optical Crystals, *Inorg. Chem.*, 2021, **60**, 8103–8110.
19 H. W. Yu, J. Young, H. P. Wu, W. G. Zhang, J. M. Rondinelli and P. S. Halasyamani, $M_4Mg_4(P_2O_7)_3$ (M = K, Rb): Structural Engineering of Pyrophosphates for Nonlinear Optical Applications, *Chem. Mater.*, 2017, **29**, 1845–1855.
20 L. Li, Y. Wang, B. H. Lei, S. J. Han, Z. H. Yang, K. R. Poeppelmeier and S. L. Pan, A New Deep-Ultraviolet Transparent Orthophosphate $LiCs_2PO_4$ with Large Second Harmonic Generation Response, *J. Am. Chem. Soc.*, 2016, **138**, 9101–9104.
21 S. G. Zhao, X. Y. Yang, Y. Yang, X. J. Kuang, F. Q. Lu, P. Shan, Z. H. Sun, Z. S. Lin, M. C. Hong and J. H. Luo, Non-Centrosymmetric $RbNaMgP_2O_7$ with Unprecedented Thermo-Induced Enhancement of Second Harmonic Generation, *J. Am. Chem. Soc.*, 2018, **140**, 1592–1595.
22 T. Baiheti, S. J. Han, A. Tudi, Z. H. Yang and S. L. Pan, Alignment of Polar Moieties Leading to Strong Second Harmonic Response in $KCsMoP_2O_9$, *Chem. Mater.*, 2020, **32**, 3297–3303.
23 C. Wu, X. X. Jiang, Y. L. Hu, C. B. Jiang, T. H. Wu, Z. S. Lin, Z. P. Huang, M. G. Humphrey and C. Zhang, A Lanthanum Ammonium Sulfate Double Salt with a Strong SHG Response and Wide Deep-UV Transparency, *Angew. Chem., Int. Ed.*, 2022, **61**, e202115855.
24 S. G. Zhao, P. F. Gong, S. Y. Luo, L. Bai, Z. S. Lin, C. M. Ji, T. L. Chen, M. C. Hong and J. H. Luo, Deep-Ultraviolet Transparent Phosphates $RbBa_2(PO_3)_5$ and $Rb_2Ba_3(P_2O_7)_2$ Show Nonlinear Optical Activity from Condensation of $[PO_4]^{3-}$ Units, *J. Am. Chem. Soc.*, 2014, **136**, 8560–8563.
25 C. Wu, G. F. Wei, X. X. Jiang, Q. K. Xu, Z. S. Lin, Z. P. Huang, M. G. Humphrey and C. Zhang, Additive-Triggered Polar Polymorph Formation: β-$Sc(IO_3)_3$, a Promising Next-Generation Mid-Infrared Nonlinear Optical Material, *Angew. Chem., Int. Ed.*, 2022, **61**, e202208514.
26 M. Luo, C. S. Lin, D. H. Lin and N. Ye, Rational Design of the Metal-Free $KBe_2BO_3F_2{\cdot}$(KBBF) Family Member $C(NH_2)_3SO_3F$ with Ultraviolet Optical Nonlinearity, *Angew. Chem., Int. Ed.*, 2020, **59**, 15978–15981.
27 T. H. Wu, X. X. Jiang, C. Wu, Y. L. Hu, Z. S. Lin, Z. P. Huang, M. G. Humphrey and C. Zhang, Ultrawide Bandgap and Outstanding Second-Harmonic Generation Response by a Fluorine-Enrichment Strategy at a Transition-Metal Oxyfluoride Nonlinear Optical Material, *Angew. Chem., Int. Ed.*, 2022, **61**, e202203104.
28 L. L. Wu, C. S. Lin, H. T. Tian, Y. Q. Zhou, H. X. Fan, S. D. Yang, N. Ye and M. Luo, $Mg(C_3O_4H_2)(H_2O)_2$: A New Ultraviolet Nonlinear Optical Material Derived from $KBe_2BO_3F_2$ with High Performance and Excellent Water-Resistance, *Angew. Chem., Int. Ed.*, 2024, **63**, e202315647.
29 C. Wu, C. B. Jiang, G. F. Wei, X. X. Jiang, Z. J. Wang, Z. S. Lin, Z. P. Huang, M. G. Humphrey and C. Zhang, Toward Large Second-Harmonic Generation and Deep-UV Transparency in Strongly Electropositive Transition Metal Sulfates, *J. Am. Chem. Soc.*, 2023, **145**, 3040–3046.
30 Y. Q. Li, W. Q. Huang, Y. Zhou, X. Y. Song, J. Y. Zheng, H. Wang, Y. P. Song, M. J. Li, J. H. Luo and S. G. Zhao, A High-Performance Nonlinear Optical Crystal with a Building Block Containing Expanded π-Delocalization, *Angew. Chem., Int. Ed.*, 2023, **62**, e202215145.
31 C. Wu, T. H. Wu, X. X. Jiang, Z. J. Wang, H. Y. Sha, L. Lin, Z. S. Lin, Z. P. Huang, X. F. Long, M. G. Humphrey and C. Zhang, Large Second-Harmonic Response and Giant Birefringence of $CeF_2(SO_4)$ Induced by Highly Polarizable Polyhedra, *J. Am. Chem. Soc.*, 2021, **143**, 4138–4142.
32 C. B. Jiang, X. X. Jiang, C. Wu, Z. P. Huang, Z. S. Lin, M. G. Humphrey and C. Zhang, Isoreticular Design of $KTiOPO_4$-Like Deep-Ultraviolet Transparent Materials Exhibiting Strong Second-Harmonic Generation, *J. Am. Chem. Soc.*, 2022, **144**, 20394–20399.
33 Y. L. Hu, C. Wu, X. X. Jiang, Z. J. Wang, Z. P. Huang, Z. S. Lin, X. F. Long, M. G. Humphrey and C. Zhang, Giant Second-Harmonic Generation Response and Large Band Gap in the Partially Fluorinated Mid-Infrared Oxide $RbTeMo_2O_8F$, *J. Am. Chem. Soc.*, 2021, **143**, 12455–12459.
34 C. C. Jin, X. X. Jiang, C. Wu, K. N. Duanmu, Z. S. Lin, Z. P. Huang, M. G. Humphrey and C. Zhang, Giant Mid-Infrared Second-Harmonic Generation Response in a Densely-Stacked Van Der Waals Transition-Metal Oxychloride, *Angew. Chem., Int. Ed.*, 2023, **62**, e202310835.
35 T. Y. Fan, C. E. Huang, B. Q. Hu, R. C. Eckardt, Y. X. Fan, R. L. Byer and R. S. Feigelson, Second harmonic generation and accurate index of refraction measurements in flux-grown $KTiOPO_4$, *Appl. Opt.*, 1987, **26**, 2390–2394.
36 D. N. Nikogosyan, *Nonlinear Optical Crystals: A Complete Survey*, Springer, New York, 2005.
37 Z. Y. Lv and R. K. Li, Synthesis, Crystal Structure, and Characterizations of Two Tantalum Phosphates $A_3TaP_2O_9$ (A = K, Na), *Inorg. Chem.*, 2022, **61**, 13554–13560.
38 H. N. Liu, H. P. Wu, H. W. Yu, Z. G. Hu, J. Y. Wang and Y. C. Wu, $K_2ZnMoP_2O_{10}$: a novel nonlinear optical molybdophosphate with a strong second harmonic generation response and moderate birefringence, *J. Mater. Chem. C*, 2021, **9**, 15321–15328.
39 Z. Y. Lv and R. K. Li, $Na_{12}(NbO)_3(PO_4)_7$: A Congruent Melting Nonlinear Optical Crystal with Large NbO_6 Distortion and High Laser-Induced Damage Threshold, *Inorg. Chem.*, 2024, **63**, 3610–3615.

Published on 22 Oktober 2024. Downloaded on 14.10.25 16:33:10.

40 X. F. Lu, Z. H. Chen, X. R. Shi, Q. Jing and M. H. Lee, Two Pyrophosphates with Large Birefringences and Second-Harmonic Responses as Ultraviolet Nonlinear Optical Materials, *Angew. Chem., Int. Ed.*, 2020, **59**, 17648–17656.
41 L. Qi, Z. H. Chen, X. R. Shi, X. D. Zhang, Q. Jing, N. Li, Z. Q. Jiang, B. B. Zhang and M. H. Lee, $A_3BBi(P_2O_7)_2$ (A = Rb, Cs; B = Pb, Ba): Isovalent Cation Substitution to Sustain Large Second-Harmonic Generation Responses, *Chem. Mater.*, 2020, **32**, 8713–8723.
42 Y. L. Deng, L. Huang, X. H. Dong, L. Wang, K. M. Ok, H. M. Zeng, Z. E. Lin and G. H. Zou, $K_2Sb(P_2O_7)F$: Cairo Pentagonal Layer with Bifunctional Genes Reveal Optical Performance, *Angew. Chem., Int. Ed.*, 2020, **59**, 21151–21156.
43 X. H. Dong, H. B. Huang, L. Huang, Y. Q. Zhou, B. B. Zhang, H. M. Zeng, Z. E. Lin and G. H. Zou, Unearthing Superior Inorganic UV Second-Order Nonlinear Optical Materials: A Mineral-Inspired Method Integrating First-Principles High-Throughput Screening and Crystal Engineering, *Angew. Chem., Int. Ed.*, 2024, **63**, e202318976.
44 T. Zheng, Q. Wang, J. X. Ren, L. L. Cao, L. Huang, D. J. Gao, J. Bi and G. H. Zou, Halogen regulation triggers structural transformation from centrosymmetric to noncentrosymmetric switches in tin phosphate halides Sn_2PO_4X (X = F, Cl), *Inorg. Chem. Front.*, 2022, **9**, 4705–4713.
45 Y. L. Sun, G. X. Liu, Y. L. Lv, L. Ma, W. D. Yao and R. L. Tang, $(NH_4)_3(H_3O)Zn_4(PO_4)_4$: A nonlinear optical zinc orthophosphate crystal, *J. Solid State Chem.*, 2023, **325**, 124171.
46 B. L. Wu, C. L. Hu, F. F. Mao, R. L. Tang and J. G. Mao, Highly Polarizable Hg^{2+} Induced a Strong Second Harmonic Generation Signal and Large Birefringence in $LiHgPO_4$, *J. Am. Chem. Soc.*, 2019, **141**, 10188–10192.
47 B. H. Lei, Z. H. Yang, H. W. Yu, C. Cao, Z. Li, C. Hu, K. R. Poeppelmeier and S. L. Pan, Module-Guided Design Scheme for Deep-Ultraviolet Nonlinear Optical Materials, *J. Am. Chem. Soc.*, 2018, **140**, 10726–10733.
48 A. L. Aleksandrovskiĭ, S. A. Akhmanov, A. D. Vladimir, N. I. Zheludev and I. P. Vladimir, Efficient nonlinear optical converters made of potassium titanyl phosphate crystals, *Sov. J. Quantum Electron.*, 1985, **15**, 885.
49 X. Wen, C. S. Lin, M. Luo, H. X. Fan, K. C. Chen and N. Ye, $[C(NH_2)_3]_3PO_4{\cdot}2H_2O$: A new metal-free ultraviolet nonlinear optical phosphate with large birefringence and second-harmonic generation response, *Sci. China Mater.*, 2021, **64**, 2008–2016.
50 J. Lu, X. Liu, M. Zhao, X. B. Deng, K. X. Shi, Q. R. Wu, L. Chen and L. M. Wu, Discovery of NLO Semiorganic $(C_5H_6ON)^+(H_2PO_4)^-$: Dipole Moment Modulation and Superior Synergy in Solar-Blind UV Region, *J. Am. Chem. Soc.*, 2021, **143**, 3647–3654.
51 Z. P. Zhang, X. Liu, X. M. Liu, Z. W. Lu, X. Sui, B. Y. Zhen, Z. S. Lin, L. Chen and L. M. Wu, Driving Nonlinear Optical Activity with Dipolar 2-Aminopyrimidinium Cations in $(C_4H_6N_3)^+(H_2PO_3)^-$, *Chem. Mater.*, 2022, **34**, 1976–1984.
52 L. Xiong, J. Chen, J. Lu, C. Y. Pan and L. M. Wu, Monofluorophosphates: A New Source of Deep-Ultraviolet Nonlinear Optical Materials, *Chem. Mater.*, 2018, **30**, 7823–7830.
53 S. F. Li, L. Hu, Y. Ma, F. F. Mao, J. Zheng, X. D. Zhang and D. Yan, Noncentrosymmetric $(C_3H_7N_6)_6(H_2PO_4)_4(HPO_4){\cdot}4H_2O$ and Centrosymmetric $(C_3H_7N_6)_2SO_4{\cdot}2H_2O$: Exploration of Acentric Structure by Combining Planar and Tetrahedral Motifs via Hydrogen Bonds, *Inorg. Chem.*, 2022, **61**, 10182–10189.
54 L. Qi, X. X. Jiang, K. N. Duanmu, C. Wu, Z. S. Lin, Z. P. Huang, M. G. Humphrey and C. Zhang, Record Second-Harmonic Generation and Birefringence in an Ultraviolet Antimonate by Bond Engineering, *J. Am. Chem. Soc.*, 2024, **146**, 9975–9983.
55 C. Wu, X. X. Jiang, Z. J. Wang, H. Y. Sha, Z. S. Lin, Z. P. Huang, X. F. Long, M. G. Humphrey and C. Zhang, UV Solar-Blind-Region Phase-Matchable Optical Nonlinearity and Anisotropy in a π-Conjugated Cation-Containing Phosphate, *Angew. Chem., Int. Ed.*, 2021, **60**, 14806–14810.
56 G. M. Sheldrick, A short history of SHELX, *Acta Crystallogr., Sect. A: Found. Crystallogr.*, 2008, **64**, 112–122.
57 O. V. Dolomanov, L. J. Bourhis, R. J. Gildea, J. A. K. Howard and H. Puschmann, OLEX2: a complete structure solution, refinement and analysis program, *J. Appl. Crystallogr.*, 2009, **42**, 339–341.
58 G. M. Sheldrick, SHELXT – Integrated space-group and crystal-structure determination, *Acta Crystallogr., Sect. A: Found. Adv.*, 2015, **71**, 3–8.
59 A. L. Spek, PLATON SQUEEZE: a tool for the calculation of the disordered solvent contribution to the calculated structure factors, *Acta Crystallogr., Sect. C: Struct. Chem.*, 2015, **71**, 9–18.
60 S. K. Kurtz and T. T. Perry, A Powder Technique for the Evaluation of Nonlinear Optical Materials, *J. Appl. Phys.*, 1968, **39**, 3798–3813.
61 B. E. Srensen, A revised Michel-Levy interference colour chart based on first-principles calculations, *Eur. J. Mineral.*, 2013, **25**, 5–10.
62 L. L. Cao, G. Peng, W. B. Liao, T. Yan, X. F. Long and N. Ye, A microcrystal method for the measurement of birefringence, *CrystEngComm*, 2020, **22**, 1956–1961.
63 W. Kohn and L. J. Sham, Self-Consistent Equations Including Exchange and Correlation Effects, *Phys. Rev. [Sect.] A*, 1965, **140**, A1133–A1138.
64 M. C. Payne, M. P. Teter, D. C. Allan, T. A. Arias and J. D. Joannopoulos, Iterative minimization techniques for ab initio total-energy calculations: molecular dynamics and conjugate gradients, *Rev. Mod. Phys.*, 1992, **64**, 1045–1097.
65 S. J. Clark, M. D. Segall, C. J. Pickard, P. J. Hasnip, M. I. J. Probert, K. Refson and M. C. Payne, First principles methods using CASTEP, *Z. Kristallogr.*, 2005, **220**, 567–570.
66 J. P. Perdew, K. Burke and M. Ernzerhof, Generalized Gradient Approximation Made Simple, *Phys. Rev. Lett.*, 1996, **77**, 3865–3868.

 This journal is © the Partner Organisations 2024

Published on 22 Oktober 2024. Downloaded on 14.10.25 16:33:10.

67 J. P. Perdew and Y. Wang, Pair-distribution function and its coupling-constant average for the spin-polarized electron gas, *Phys. Rev. B: Condens. Matter Mater. Phys.*, 1992, **46**, 12947–12954.
68 H. J. Monkhorst and J. D. Pack, Special points for Brillouin-zone integrations, *Phys. Rev. B: Solid State*, 1976, **13**, 5188–5192.
69 R. W. Godby, M. Schlüter and L. J. Sham, Self-energy operators and exchange-correlation potentials in semiconductors, *Phys. Rev. B: Condens. Matter Mater. Phys.*, 1988, **37**, 10159–10175.
70 S. D. Mo and W. Y. Ching, Electronic and optical properties of three phases of titanium dioxide: Rutile, anatase, and brookite, *Phys. Rev. B: Condens. Matter Mater. Phys.*, 1995, **51**, 13023–13032.
71 S. Laksari, A. Chahed, N. Abbouni, O. Benhelal and B. Abbar, First-principles calculations of the structural, electronic and optical properties of $CuGaS_2$ and $AgGaS_2$, *Comput. Mater. Sci.*, 2006, **38**, 223–230.
72 D. A. Kleinman, Nonlinear Dielectric Polarization in Optical Media, *Phys. Rev.*, 1962, **126**, 1977–1979.
73 C. Aversa and J. E. Sipe, Nonlinear optical susceptibilities of semiconductors: Results with a length-gauge analysis, *Phys. Rev. B: Condens. Matter Mater. Phys.*, 1995, **52**, 14636–14645.
74 S. N. Rashkeev, W. R. L. Lambrecht and B. Segall, Efficient ab initio method for the calculation of frequency-dependent second-order optical response in semiconductors, *Phys. Rev. B: Condens. Matter Mater. Phys.*, 1998, **57**, 3905–3919.
75 M. H. Lee, C. H. Yang and J. H. Jan, Band-resolved analysis of nonlinear optical properties of crystalline and molecular materials, *Phys. Rev. B: Condens. Matter Mater. Phys.*, 2004, **70**, 235110.
76 J. Lin, M. H. Lee, Z. P. Liu, C. T. Chen and C. J. Pickard, Mechanism for linear and nonlinear optical effects in β-BaB_2O_4 crystals, *Phys. Rev. B: Condens. Matter Mater. Phys.*, 1999, **60**, 13380–13389.
77 M. J. Frisch, *Gaussian 16, Rev. C.01*, 2016.
78 R. M. Hill and S. K. Ichiki, Infrared Absorption by Hydrogen Bonds in Single Crystal KH_2PO_4, KD_2PO_4, and KH_2AsO_4, *J. Chem. Phys.*, 1968, **48**, 838–842.
79 G. Socrates, *Infrared and Raman Characteristic Group Frequencies: Tables and Charts*, Wiley, 2004.
80 W. M. Wendlandt and H. G. Hecht, *Reflectance Spectroscopy*, Interscience, New York, 1966.
81 J. Tauc, Absorption edge and internal electric fields in amorphous semiconductors, *Mater. Res. Bull.*, 1970, **5**, 721–729.
82 C. H. Hu, C. J. Shen, H. Zhou, J. Han, Z. H. Yang, K. R. Poeppelmeier, F. Zhang and S. L. Pan, $(C_3N_2H_5)B_3O_3F_2(OH)_2$: Realizing Large Birefringence via a Synergistic Effect between Anion F/OH-Ratio Optimization and Cation Activation, *Small Struct.*, 2024, 2400296.
83 V. G. Dmitriev, G. G. Gurzadyan and D. N. Nikogosyan, *Handbook of Nonlinear Optical Crystals*, Springer, Berlin, 1999.
84 J. Lu, J. N. Yue, L. Xiong, W. K. Zhang, L. Chen and L. M. Wu, Uniform Alignment of Non-π-Conjugated Species Enhances Deep Ultraviolet Optical Nonlinearity, *J. Am. Chem. Soc.*, 2019, **141**, 8093–8097.
85 X. Y. Cheng, M. H. Whangbo, G. C. Guo, M. C. Hong and S. Q. Deng, The Large Second-Harmonic Generation of $LiCs_2PO_4$ is caused by the Metal-Cation-Centered Groups, *Angew. Chem., Int. Ed.*, 2018, **57**, 3933–3937.
86 R. W. Godby, M. Schlüter and L. J. Sham, Trends in self-energy operators and their corresponding exchange-correlation potentials, *Phys. Rev. B: Condens. Matter Mater. Phys.*, 1987, **36**, 6497–6500.
87 D. Eimerl, S. Velsko, L. Davis, F. Wang, G. Loiacono and G. Kennedy, Deuterated L-arginine phosphate: a new efficient nonlinear crystal, *IEEE J. Quantum Electron.*, 1989, **25**, 179–193.